Supplementary Materials

Transparent porous polymer sheets for efficient product separation in solar water splitting

Ciler Özen[a], Keisuke Obata[a], Peter Bogdanoff[a], Nursidik Yulianto[b,c], Hutomo Suryo Wasisto[b,d] and Fatwa F. Abdi[a,*]

[a] Institute for Solar Fuels, Helmholtz-Zentrum Berlin für Materialien und Energie GmbH, Hahn-Meitner-Platz 1, 14109 Berlin, Germany

[b] Institute of Semiconductor Technology (IHT) and Laboratory for Emerging Nanometrology (LENA), Technische Universität Braunschweig, Braunschweig 38106, Germany

[c] Research Center for Physics, National Research and Innovation Agency (BRIN), Jl. Kawasan Puspiptek No. 441-442, South Tangerang 15314, Indonesia

[d] PT Nanosense Instrument Indonesia, Umbulharjo, Yogyakarta 55167, Indonesia

[*] Correspondence: fatwa.abdi@helmholtz-berlin.de

Table S1. Polymer separators with various microhole array dimensions used in our experiments, as fabricated by femtosecond laser micromachining technique.

Material	Thickness (μm)	Intended porosity	Hole diameter (μm)	Pitch (μm)	Obtained Porosity
Mylar	23	0.2	143.36 ± 3.54	234.43 ± 5.21	0.29 ± 0.05
Mylar	23	0.2	442.13 ± 1.90	793.20 ± 30.00	0.24 ± 0.05
Mylar	75	0.2	141.56 ± 3.07	237.10 ± 2.97	0.28 ± 0.04
Mylar	75	0.09	112.71 ± 2.60	352.02 ± 7.10	0.08 ± 0.04
Mylar	75	0.03	112.71 ± 2.60	512.00 ± 3.00	0.04 ± 0.01
Mylar	125	0.2	92.00 ± 4.18	228.15 ± 2.48	0.13 ± 0.07
Mylar	125	0.09	95.03 ± 4.01	303.12 ± 0.01	0.08 ± 0.06
Mylar	125	0.03	97.03 ± 3.07	504.59 ± 3.39	0.03 ± 0.05
Mylar	125	0.2	430.37 ± 2.22	817.37 ± 10.01	0.22 ± 0.02
FEP	25	0.2	428.85 ± 1.00	826.69 ± 5.10	0.21 ± 0.01
FEP	127	0.2	428.99 ± 1.92	826.69 ± 8.98	0.21 ± 0.02

Table S2. Baseline parameters used in the electrochemical simulation. Unless specifically mentioned in the manuscript text or figure captions, the parameters here were used.

	Parameter	Value	Ref.
Electrolyte	Initial H^+ concentration, $c_{H^+,i}$	10^{-7} M (pH = 7)	
	Initial HPO_4^{2-} concentration, $c_{HPO_4^{2-},i}$	0.076 M	
	Initial $H_2PO_4^-$ concentration, $c_{H_2PO_4^-,i}$	0.051 M	
	Initial dissolved O_2 concentration, $c_{O_2,i}$	0 M	
	Initial dissolved H_2 concentration, $c_{H_2,i}$	0 M	
	Diffusivity of H^+, D_{H^+}	9.3×10^{-9} m^2/s	[1, 2]
	Diffusivity of K^+, D_{K^+}	1.96×10^{-9} m^2/s	[1, 2]
	Diffusivity of HPO_4^{2-}, $D_{HPO_4^{2-}}$	0.69×10^{-9} m^2/s	[1]
	Diffusivity of $H_2PO_4^-$, $D_{H_2PO_4^-}$	0.85×10^{-9} m^2/s	[1]
	Buffer equilibrium constant, K_{eq}	1.5×10^{-4} mol/m^3	[3]
	Diffusivity of O_2, D_{O_2}	2.4×10^{-9} m^2/s	[1]
	Diffusivity of H_2, D_{H_2}	5×10^{-9} m^2/s	[1]
	Inlet velocity, u_{in}	1 cm/s	
	Outlet pressure, p_{out}	10^5 Pa	
	Dynamic viscosity, μ	0.89 mPa s	[1]
	Density, ρ	998.5 kg/m^3	[1]
	Temperature	300 K	
Electrode	HER exchange current density, $i_{0,HER}$	10 A/m^2	[4, 5]
	HER anodic transfer coefficient, $\alpha_{a,HER}$	0.5	
	HER cathodic transfer coefficient, $\alpha_{c,HER}$	0.5	
	OER exchange current density, $i_{0,OER}$	10^{-4} A/m^2	[4],[6-8]
	OER anodic transfer coefficient, $\alpha_{a,OER}$	1.9	
	OER cathodic transfer coefficient, $\alpha_{c,OER}$	0.1	
	Electrode conductivity, σ_{el}	10^5 S/m	
	Applied average current density, j_{app}	1 mA/cm^2	
	Equilibrium potential for water oxidation	1.23 V	
	Equilibrium potential for water reduction	0 V	
Geometry	Cell height, h_{cell}	3 cm	
	Cell width, w_{cell}	1.8 cm	
	Electrode height, h_{el}	2.7 cm	
	Separator thickness, d_{sep}	125 µm	
	Porosity	0.2	
	Pore diameter, d_{pore}	400 µm	

Table S3. Baseline parameters used in the particle tracing simulation. Unless specifically mentioned in the manuscript text or figure captions, the parameters here were used.

Parameter	Value	Ref.
Bubble formation efficiency, η_{bubble}	0.5	
Tilt condition, θ	30°	
Bubble diameter, d_p	0.1 mm	[9]
Density of O_2 gas, ρ_G	1.3 kg/m^3	
Local current density, j_s	10 mA/cm^2	

Supplementary note 1: Descriptions of our electrochemical model

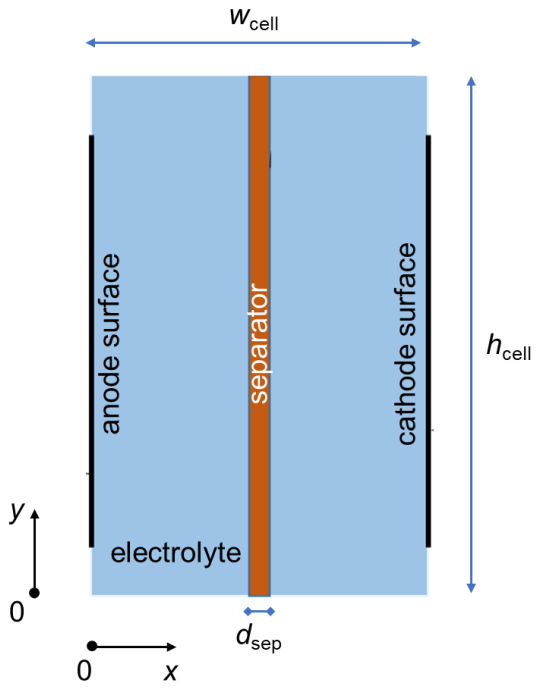

Figure S1: 2D schematic of the domains considered in our electrochemical model, which corresponds experimental cell setup. Unless otherwise mentioned, h_{cell} is 3 cm, and w_{cell} is 1.8 cm. d_{sep} is the thickness of the separator, which is varied in our simulations based on experiments.

Figure S1 shows the schematic of the two-dimensional (2-D) domains considered in our numerical model of electrochemical water splitting device with transparent separator, which is based on the experimental setup. The baseline parameters used in the model is listed in Table S2. The steady-state governing transport (Nernst-Planck) and conservation equations of the ionic species, considering charge neutrality are considered in the electrolyte domain:

$$-\nabla.\mathbf{N_i} + R_i = 0 \tag{S1}$$

$$\mathbf{N_i} = -D_i\nabla c_i - \frac{z_i D_i}{RT} F c_i \nabla \phi_l + c_i \mathbf{u} \tag{S2}$$

Here, $\mathbf{N_i}$ is the molar flux vector, R_i is the reaction source term, D_i is the diffusivity, c_i is the concentration, and z_i is the charge of species i. F is Faraday's constant, ϕ_l is the electrolyte potential and $\mathbf{u}$ is the electrolyte velocity vector. The above equations apply for H^+, K^+, HPO_4^{2-} and $H_2PO_4^-$ in our study. Local equilibrium of buffer species (i.e., H^+, HPO_4^{2-} and $H_2PO_4^-$) was also assumed based on the equilibrium constant K_{eq}. For the dissolved neutral species (i.e., H_2 and O_2), equation S2 is simplified to the diffusion-advection equation where $z_i = 0$. Laminar flow within the device was described mathematically by continuity and momentum (Navier-Stokes equation) conservation:

$$\nabla . \mathbf{u} = 0 \tag{S3}$$

$$\rho \mathbf{u} . \nabla \mathbf{u} = -\nabla p + \mu \nabla^2 \mathbf{u} + \rho \mathbf{g} \tag{S4}$$

ρ is the density, p is the pressure, μ is the viscosity and $\mathbf{g}$ is gravity. At the electrode surface, mass fluxes were determined by the local current density (i_{loc}) and the stoichiometry coefficients (ν_i) of the redox equilibrium reaction:

$$\nu_{Ox} Ox + ne^- \rightleftharpoons \nu_{Red} Red \tag{S5}$$

$$R_i = \frac{-\nu_i i_{loc}}{nF} \tag{S6}$$

The stoichiometry coefficients for H^+, H_2, and O_2 are −4, 2, and −1, respectively, when the number of electrons (n) is 4. The local electrode current density (i_{loc}) was determined by Butler-Volmer equation:

$$i_{loc} = j_0 \left\{ exp\left(\frac{\alpha_a F \eta}{RT}\right) - exp\left(\frac{-\alpha_c F \eta}{RT}\right) \right\} \tag{S7}$$

j_0, α_a and α_c are exchange current density, anodic and cathodic transfer coefficient, respectively. The thickness of the electrodes was neglected in our model (i.e., no Ohmic substrate loss).

The overpotential (η) for the anode and cathode was determined by:

$$\eta_{\text{anode}} = \phi_{\text{s}} - \phi_{\text{l}} - 1.23 + \frac{RT}{nF} \ln \left[\frac{c_{\text{H}^+}}{c_{\text{H}^+,\text{bulk}}} \right]^{v_i} \quad \text{(S8)}$$

$$\eta_{\text{cathode}} = \phi_{\text{s}} - \phi_{\text{l}} - 0 + \frac{RT}{nF} \ln \left[\frac{c_{\text{H}^+}}{c_{\text{H}^+,\text{bulk}}} \right]^{v_i} \quad \text{(S9)}$$

Here, ϕ_{s} is the electrode surface potential. Average current density (j_{app}) was applied at the anode, and the potential of the cathode was set to ground. On other boundaries, an insulation boundary condition (**-n**.$\mathbf{i}_{\text{l}}$ = 0, **-n**.$\mathbf{i}_{\text{s}}$ = 0) was considered.

The bottom of the cell is set as the electrolyte inlet for laminar flow with a constant inlet velocity (**u** = -u_{in}**n**); the concentration of the species at this boundary is set as the initial concentration (c = $c_{0,i}$). The top of the cell is the outlet of the cell (constant pressure and $\mathbf{n}.D_i\nabla c_i = 0$). On the side walls of the cell, no flux (**-n**.**J** = 0) and no slip (**u** = 0) boundary conditions were considered.

A mesh independence study was carried out and 98,476 triangular elements were used for a converging solution (Figure S2). Quadratic discretization method for the mass balance equation was employed to increase the accuracy of the solution. For the solutions of the dependent variables (p, u, ϕ_{l}, ϕ_{s}, c_{H^+}, $c_{\text{HPO}_4^{2-}}$, $c_{\text{H}_2\text{PO}_4^-}$, c_{O_2}, c_{H_2}), the MUMPS solver, which is a direct method based on lower-upper (LU) factorization (matrix triangulation), was used.

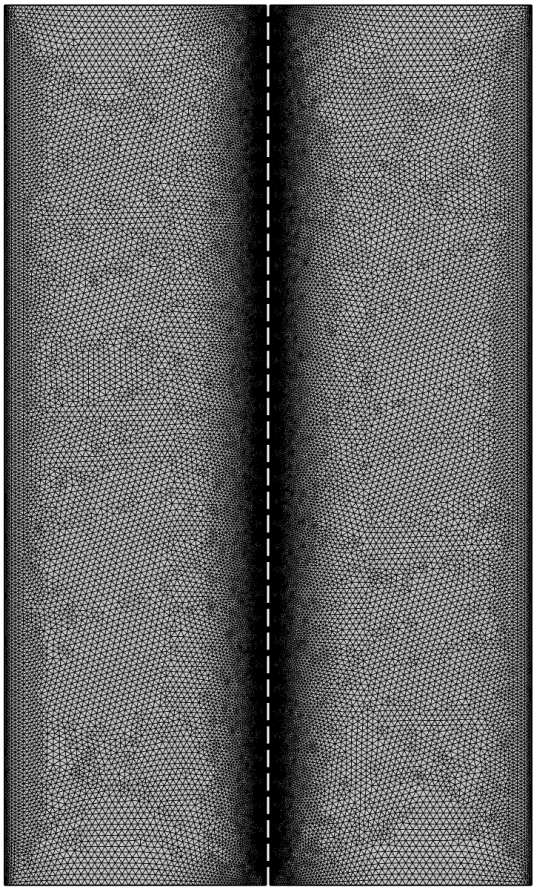

Figure S2: The optimized mesh used in our study for a converging solution. 98,476 triangular elements were created within the electrochemical cell domain. Cell height, h_{cell} = 3 cm, width, w_{cell} = 1.8 cm, separator thickness, d_{sep} = 125 μm.

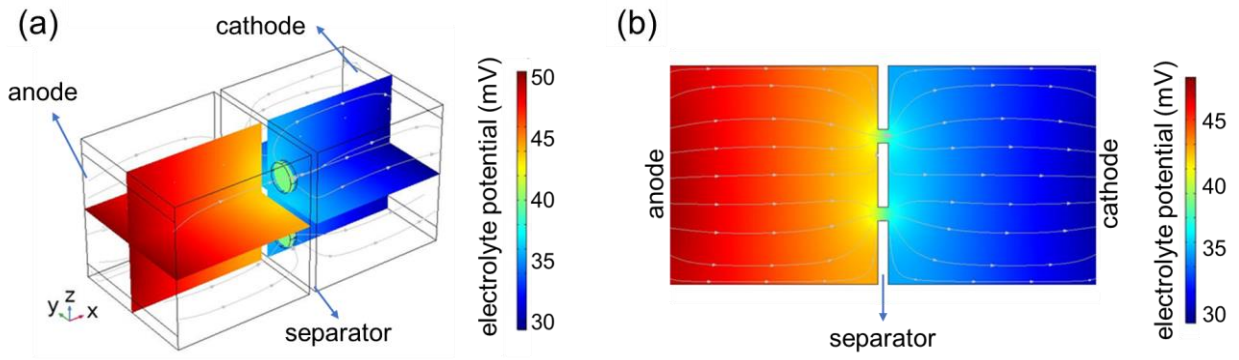

Figure S3. A comparison between the 2D model described in Supplementary Note S1 and an equivalent 3D electrochemical model with the same boundary conditions and parameters. Smaller domain sizes are considered to limit the computational expense. The electrolyte potential distributions in the cell simulated with the **(a)** 3D and **(b)** 2D models are shown. The applied current density is 1 mA/cm^2. Negligible differences are observed between the 3D and 2D results, which justifies the use of the 2D model in our study.

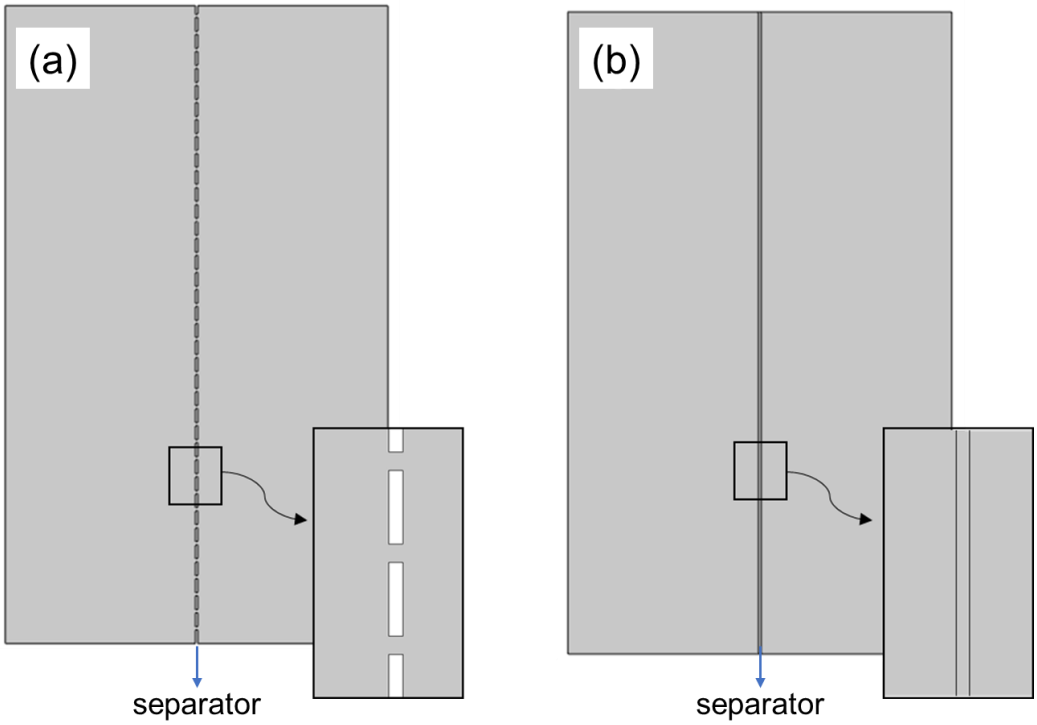

Figure S4. Two different approaches are considered in introducing porosity to the separators in the electrochemical model. **(a)** Approach 1: individual pores are considered, i.e., the separator is divided into solid and liquid domains, and only the liquid domain is evaluated. **(b)** Approach 2: a single domain is considered for the separator, and the porosity is included using Bruggeman correction. All parameters are identical for the two approaches. Pore diameter = 400 µm, separator thickness = 125 µm, porosity = 0.2.

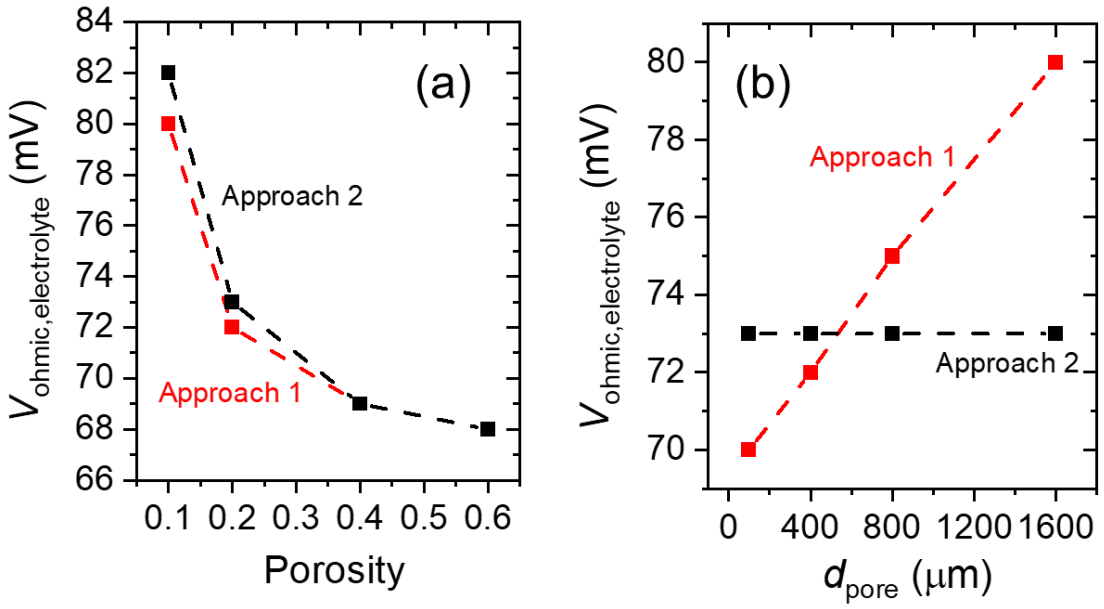

Figure S5. The effect of **(a)** porosity and **(b)** pore diameter to the electrolyte Ohmic loss when approaches 1 and 2 (as shown in Fig. S4) are considered. In all cases, the applied current density is 1 mA/cm^2. The pore diameter is kept at 400 μm in (a), and the porosity in (b) is maintained to be 0.2.

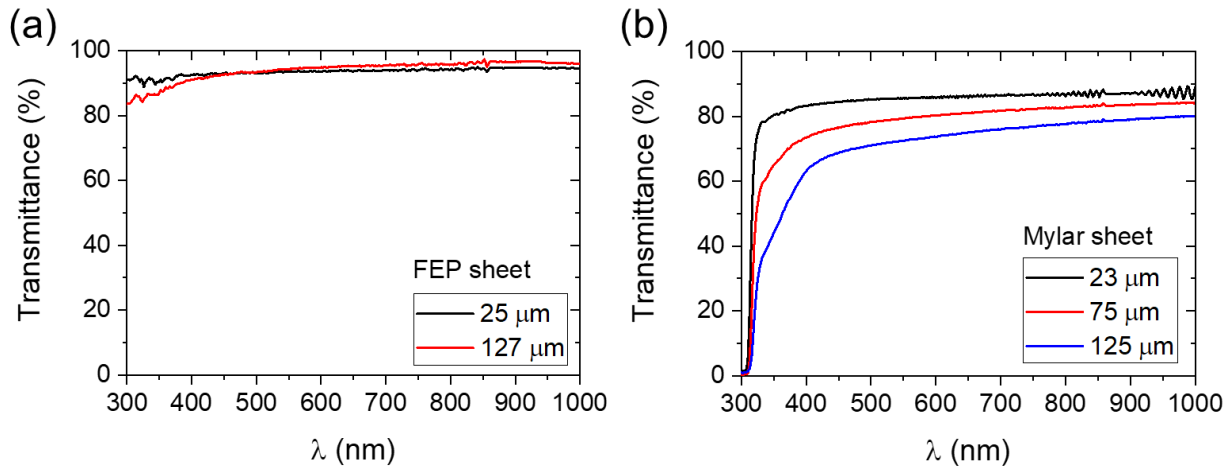

Figure S6: Transmittance spectra of **(a)** FEP and **(b)** Mylar films of various thicknesses.

Supplementary note 2: Descriptions of our particle tracing model

As described in the manuscript text, our particle tracing model considers drag and gravity forces in order to simulate oxygen gas bubbles movement as they are produced from the anode (upward-facing electrode); see equation 2 in the manuscript. The drag force, $\mathbf{F}_D$, was calculated by using Hadamard-Rybczynski drag law (equations S10 – S13), [10].

$$\mathbf{F}_D = \frac{1}{\tau_p} m_p(\mathbf{u} - \mathbf{v}) \tag{S10}$$

$$\tau_p = \frac{4\rho_p d_p^2}{3\mu C_D Re_r} \tag{S11}$$

$$C_D = \frac{8}{Re_r}\left[\frac{2+3\kappa}{1+\kappa}\right], \ \kappa = \frac{\mu_p}{\mu} \tag{S12}$$

$$Re_r = \frac{\rho\|\mathbf{u}-\mathbf{v}\| d_p}{\mu} \tag{S13}$$

τ_p, d_p, v, m_p, ρ_p and μ_p are particle response time, particle radius, particle velocity, particle mass, particle density and particle dynamic viscosity, respectively. Re_r is the particle Reynolds number. On the anode surface, flux boundary conditions were implemented, as given by equations S14 - S16.[9, 11]

$$v_{\mathrm{G},x} = \frac{j_s \eta_{\mathrm{bubble}} M}{n_e F \rho_G} \tag{S14}$$

$$R_{\mathrm{G},x} = \frac{j_s \eta_{\mathrm{bubble}} M}{n_e F} \tag{S15}$$

$$N_{m,x} = \frac{j_s (1-\eta_{\mathrm{bubble}})}{n_e F} \tag{S16}$$

$v_{\mathrm{G},x}$ is the velocity of gas bubbles, ρ_G is the density of the gas bubbles, $R_{\mathrm{G},x}$ is the mass flux of gas bubbles and $N_{m,x}$ is the molar flux of dissolved gases. η_{bubble} and j_s are the bubble formation efficiency and the local current density, respectively. F, M and n_e are the Faraday constant, the molar mass of gas (O_2 or H_2), and the number of electrons involved in the reaction, respectively. For the interaction between the bubbles and the cell, disappear boundary condition was applied at

the outlet of the cell, and bounce boundary condition ($\mathbf{v} = \mathbf{v}_c - 2(\mathbf{n}.\mathbf{v}_c)\mathbf{n}$) was implemented at the anode surface. $\mathbf{v_c}$ is the bubble velocity when striking the wall. Finally, freeze boundary condition ($\mathbf{v} = \mathbf{v}_c$) was implemented on the other walls in the cell.

Table S3 lists all the baseline parameter values used in our model. The same cell sizes as described in electrochemical model were used. Laminar flow of the electrolyte solution was considered, using the same equations and boundary conditions described for the electrochemical model (Supplementary Note 1). A total mesh of 49,972 was needed to achieve a mesh-independent solution. The mesh size was refined in the proximity of the locations where higher gradients of variables are expected.

In order to validate the model, we performed preliminary experiments using a custom cell and setup shown below in Figure S7a. Pt foil electrodes (0.05 mm, 99.99%, Alfa Aesar, product no. 42456, exposed area to the electrolyte = 2.5 cm^2) were used as the cathode and the anode, and 10 mA/cm^2 of current density between the electrodes (two-electrode configuration) was applied using a potentiostat (PARSTAT 4000A, AMETEK). A porous separator (Mylar®, d_{sep} = 125 μm, d_{pore} = 400 μm, porosity = 0.2) was placed in the cell between the cathode and the anode such that the distance between the cathode and the separator was 1.3 cm and the distance between the anode and the separator was 1.8 cm. The electrolyte was 0.1 M KP_i (pH 7), and no electrolyte flow (i.e., zero inlet velocity) was introduced to the cell. The outlets of the catholyte and anolyte compartment were connected to micro-capillary tubes that were connected to a mass spectrometer (HPR-40, HIDEN Analytical) – internal crossover of gases in the mass spectrometer and its connections were accounted for by performing control experiments. The cathode was the upward-facing electrode, and the anode was the downward-facing electrode; we therefore investigated the crossover of H_2 from the upward-facing electrode to the anolyte compartment. We acknowledge that this is

different than the simulations described in the manuscript, but this condition was chosen for the validation experiments because H_2 detection using our system is more accurate (no H_2 in the ambient air). The input parameters for the simulation (cell geometry and gas bubbles properties, such as particle mass, density, velocity) were modified accordingly for the comparison. The results of the experiments and particle tracing simulations are shown in Figure S7b for three different device angles from the horizontal plane: 30°, 45° and 90° (i.e., vertical orientation). The particle tracing simulation consistently shows lower crossover than the experimental results, but we expected this based on the following reasons: *(i)* we did not consider the possible formation of a pressure difference between the catholyte and anolyte in our model that may promote crossover; in our experiment, we tried to minimize this pressure difference but it cannot be fully excluded, *(ii)* our model only considered one-way coupling from the laminar flow to the particle dynamics and not *vice versa*; this is not expected to be an issue in the presence of forced convection (due to inlet electrolyte velocity), but this is important in the case of zero inlet velocity (as is the validation experimental condition) as a higher degree of undirected turbulence may be introduced from the bubble-electrolyte interaction, *(iii)* our model did not consider bubble-bubble interaction, which may occur during the experiment and affect the crossover, and *(iv)* constant and uniform bubble properties and bubble formation efficiency are considered in our model which is definitely not the case for the experiments. Nonetheless, the overall trend of the simulated crossover agrees with the experiment, and the discrepancy is expected to be much smaller under the conditions investigated in our manuscript (based on point *ii* above), which provides a justification for the use of our model in this study. Further experiments with dedicated cell design and configurations to better compare our simulation conditions are currently planned for more accurate validation of our model, but this is beyond the scope of the current paper.

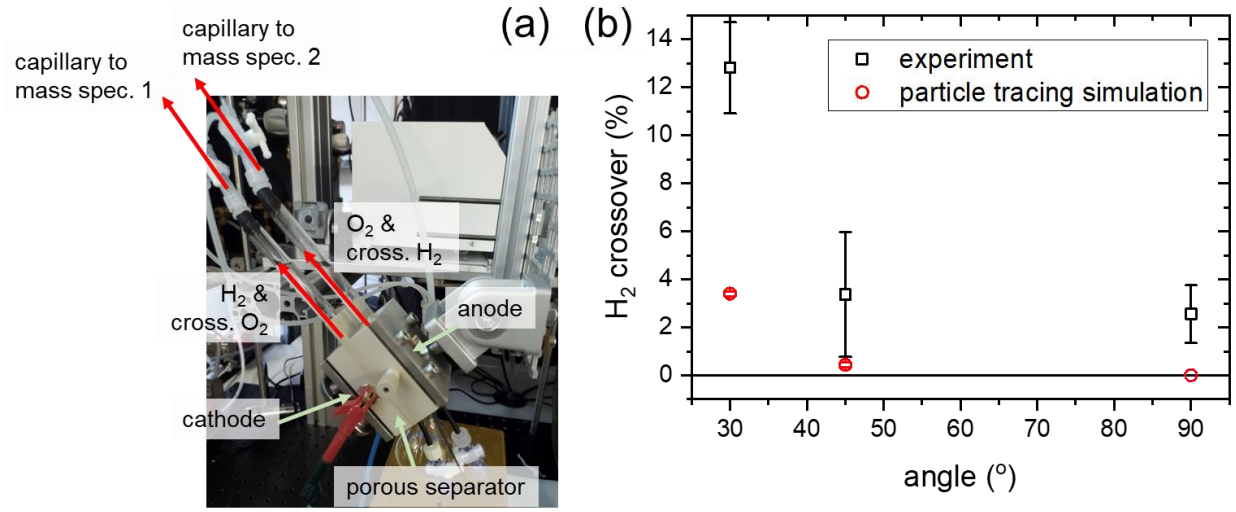

Figure S7: (a) Photograph of the cell and configuration of the product crossover validation experiments. **(b)** H_2 crossover in the anolyte compartment vs. the angle of orientation as obtained from the experiments and particle tracing simulations.

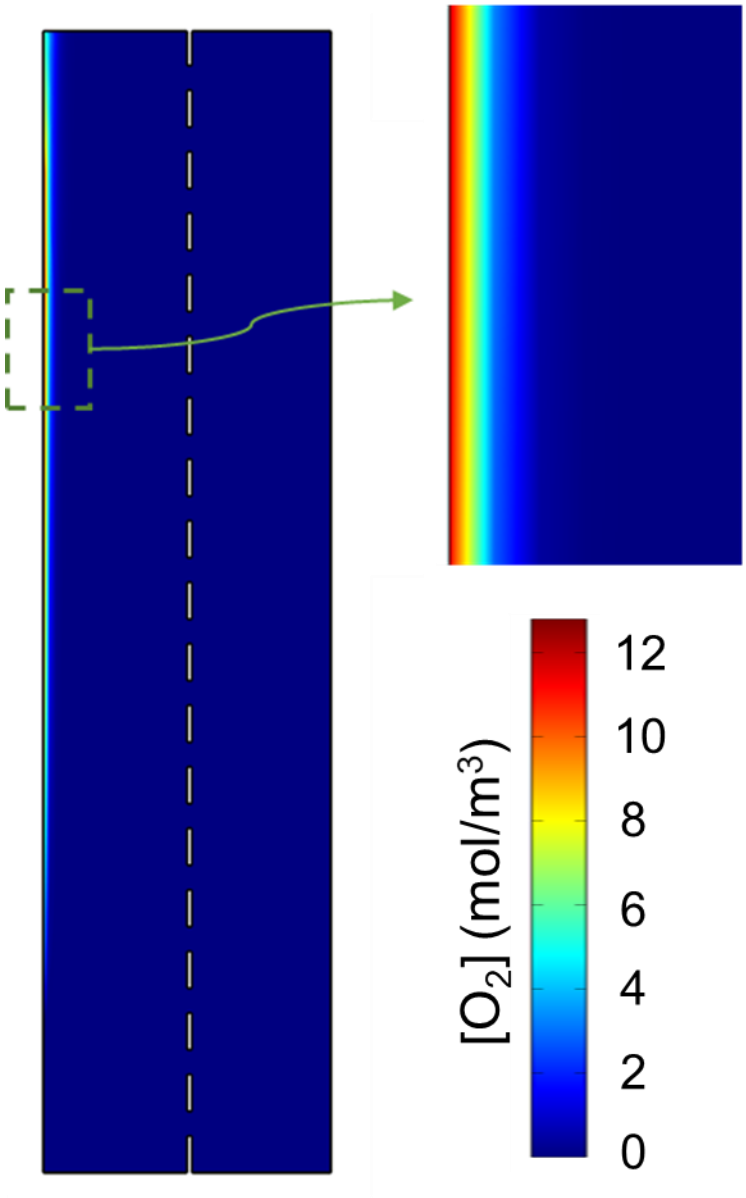

Figure S8: Dissolved O_2 concentration (mol/m^3) does not cross from the anolyte to the catholyte even in the most pessimistic case considered in our study, such as largest pore diameter (d_{pore} = 1600 µm), highest porosity value (0.4), shortest electrode distance (0.75 cm) and lower inlet velocity (1 cm/s). The applied current density is 10 mA/cm^2.

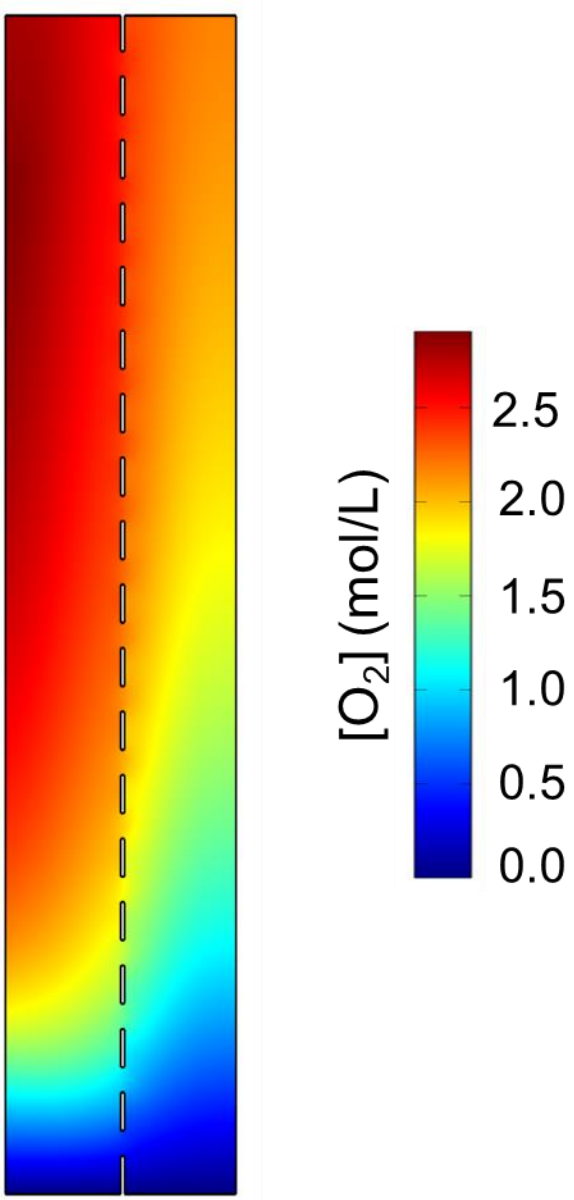

Figure S9: When no laminar flow is present (i.e., inlet velocity is zero), significant crossover of dissolved O_2 concentration (mol/L) is detected. Other than the inlet velocity, the same simulation condition as Figure S7 was applied: d_{pore} = 1600 µm, porosity = 0.4, electrode distance = 0.75 cm, and the applied current density is 10 mA/cm^2.

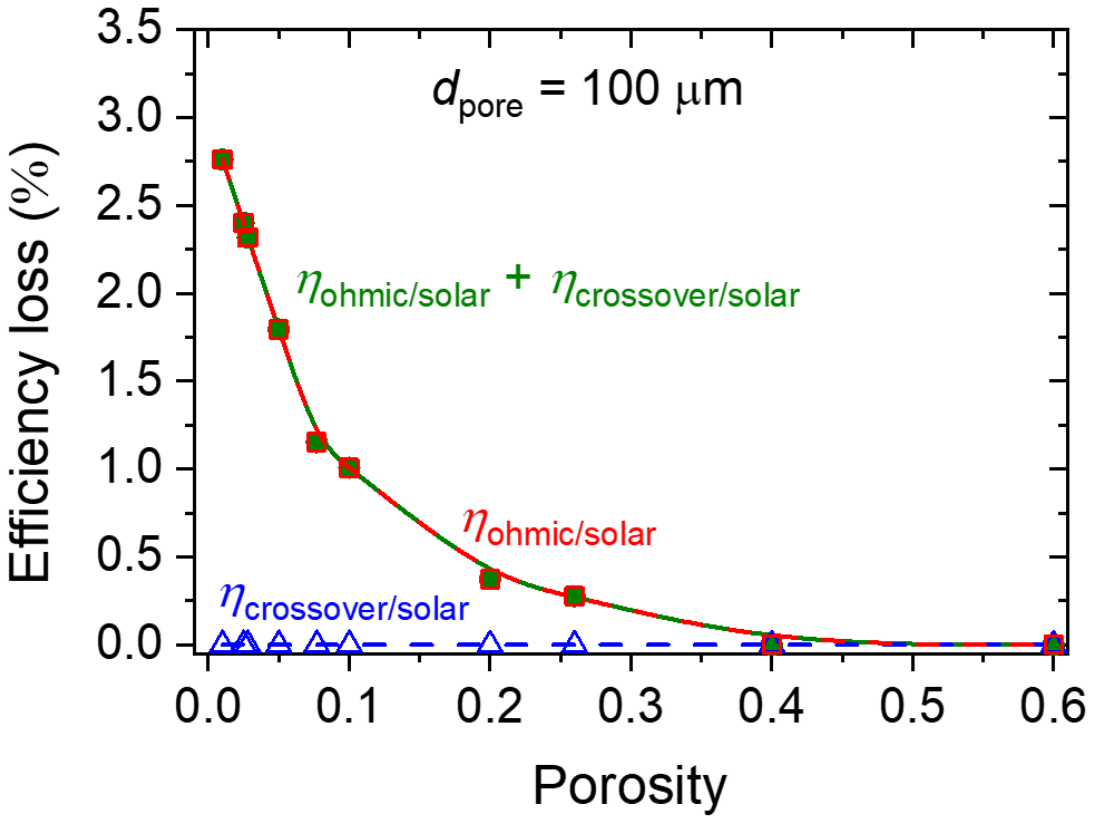

Figure S10: Total efficiency loss for various porosity values where the pore diameter (d_{pore}) is 100 μm. The total efficiency loss monotonously decreases with increasing porosity.

Movie S1: Particle tracing simulation of O_2 bubbles in a cell where the anolyte and catholyte are separated with a porous separator with a porosity of 0.2 and pore diameter of 400 μm. The scalebar depicts the velocity in m/s.


Movie S1.avi

Movie S2: Particle tracing simulation of O_2 bubbles in a cell where the anolyte and catholyte are separated with a porous separator with a porosity of 0.4 and pore diameter of 400 μm. The scalebar depicts the velocity in m/s.


Movie S2.avi

Movie S3: Particle tracing simulation of O_2 bubbles in a cell where the anolyte and catholyte are separated with a porous separator with a porosity of 0.2 and pore diameter of 800 μm. The scalebar depicts the velocity in m/s.


Movie S3.avi

REFERENCES

1. Haynes, W.M., *CRC Handbook of Chemistry and Physics*, ed. C. Press. Vol. 97th ed. 2016, FL: Boca Raton.
2. Maier, J., *Mass and charge transport involving interfaces.* Journal Of The European Ceramic Society, 1999. **19**(6-7): p. 675-681.
3. Green, A.A., *The Preparation of Acetate and Phosphate Buffer Solutions of Known pH and Ionic Strength.* J. Am. Chem. Soc, 1933. **55**: p. 2331-2336.
4. Haussener, S., et al., *Modeling, simulation, and design criteria for photoelectrochemical water-splitting systems.* Energy & Environmental Science, 2012. **5**(12): p. 9922-9935.
5. Trasatti, S., *Work function, electronegativity, and electrochemical behaviour of metals: III. Electrolytic hydrogen evolution in acid solutions.* J. Electroanal. Chem. Interf. Electrochem., 1972. **39**: p. 163-184.
6. Lodi, G., Sivieri, E., De Battisti, A. and Trasatti, S. , *Ruthenium dioxide-based film electrodes.* J. Appl. Electrochem., 1978. **8**: p. 135-143.
7. Walter, M.G., et al., *Solar Water Splitting Cells*. Chemical Reviews, 2010. **110**(11): p. 6446-6473.
8. Kinoshita, K., *Electrochemical oxygen technology*. 1992: John Wiley & Sons.
9. Holmes-Gentle, I., et al., *Optical Losses at Gas Evolving Photoelectrodes: Implications for Photoelectrochemical Water Splitting*. Journal of Physical Chemistry C, 2019. **123**(1): p. 17-28.
10. Parkinson, L., et al., *The terminal rise velocity of 10-100 mu m diameter bubbles in water*. Journal of Colloid and Interface Science, 2008. **322**(1): p. 168-172.

11. Obata, K., A. Mokeddem, and F.F. Abdi, *Multiphase fluid dynamics simulations of product crossover in solar-driven, membraneless water splitting*. Cell Reports Physical Science 2, 2021: p. 100358